Chapter 4. Young Stellar Systems

Notes:

- *Most of the material presented in this chapter is taken from Stahler and Palla (2004), Chap. 4.*

4.1 Embedded Clusters

As stars are formed deep into molecular clouds, it will be impossible to detect them at optical wavelengths because of the large amount of dust present in these environments. It should be clear from Figure 2.2 that the obscuration brought about by the dust becomes less important as one moves to longer wavelengths. As a protostar evolves it will eventually heat up the surrounding enough to heat up the dust grains to a high temperature that they will radiate efficiently in the infrared. This explains why the presence of protostars is accounted for by the presence of infrared radiation in molecular clouds.

The **infrared color-color** diagram is, therefore, very useful to located protostars according to measured fluxes in the J (1.25 μm), H (1.65 μm), and K (2.2 μm) bands (see Figure 4.1). Let us now consider the following ratio along with the necessary information that can be gathered in Figure 2.2

$$\begin{aligned}\frac{E_{J-H}}{E_{H-K}} &= \left(\frac{E_{J-V}}{E_{B-V}} - \frac{E_{H-V}}{E_{B-V}}\right)\left(\frac{E_{H-V}}{E_{B-V}} - \frac{E_{K-V}}{E_{B-V}}\right)^{-1} \\ &= \frac{2.58 - 2.25}{2.77 - 2.58} = 1.74.\end{aligned} \tag{4.1}$$

Since $E_{J-H} \equiv (J-H) - (J-H)_\circ$, etc., we find the following equation of relative reddening

$$(J-H) - (J-H)_\circ = 1.74\left[(H-K) - (H-K)_\circ\right], \tag{4.2}$$

which can be combined to the infrared color-color diagram (i.e., equation (4.2) accounts for the broken lines in Figure 4.1) to study the reddening of protostars. An example is shown in Figure 4.2 for the IC 348 embedded cluster. We see that most stars fall between the broken lines and are, therefore, seen to have a mean reddening corresponding to an extinction of $A_V \approx 5$ mag. This explains their position to the right of the main sequence curve. On the other hand, stars that fall below the lower broken line cannot be explained by reddening alone and, therefore, exhibit **infrared excess**.

When the spectral energy distribution of such stars is measured and corrected, or "dereddened", for the known amount of extinction A_V by calculating A_λ with the extinction curve (i.e., Figure 2.2), then types or classes of protostars can be identified from the corrected spectral energy distributions.

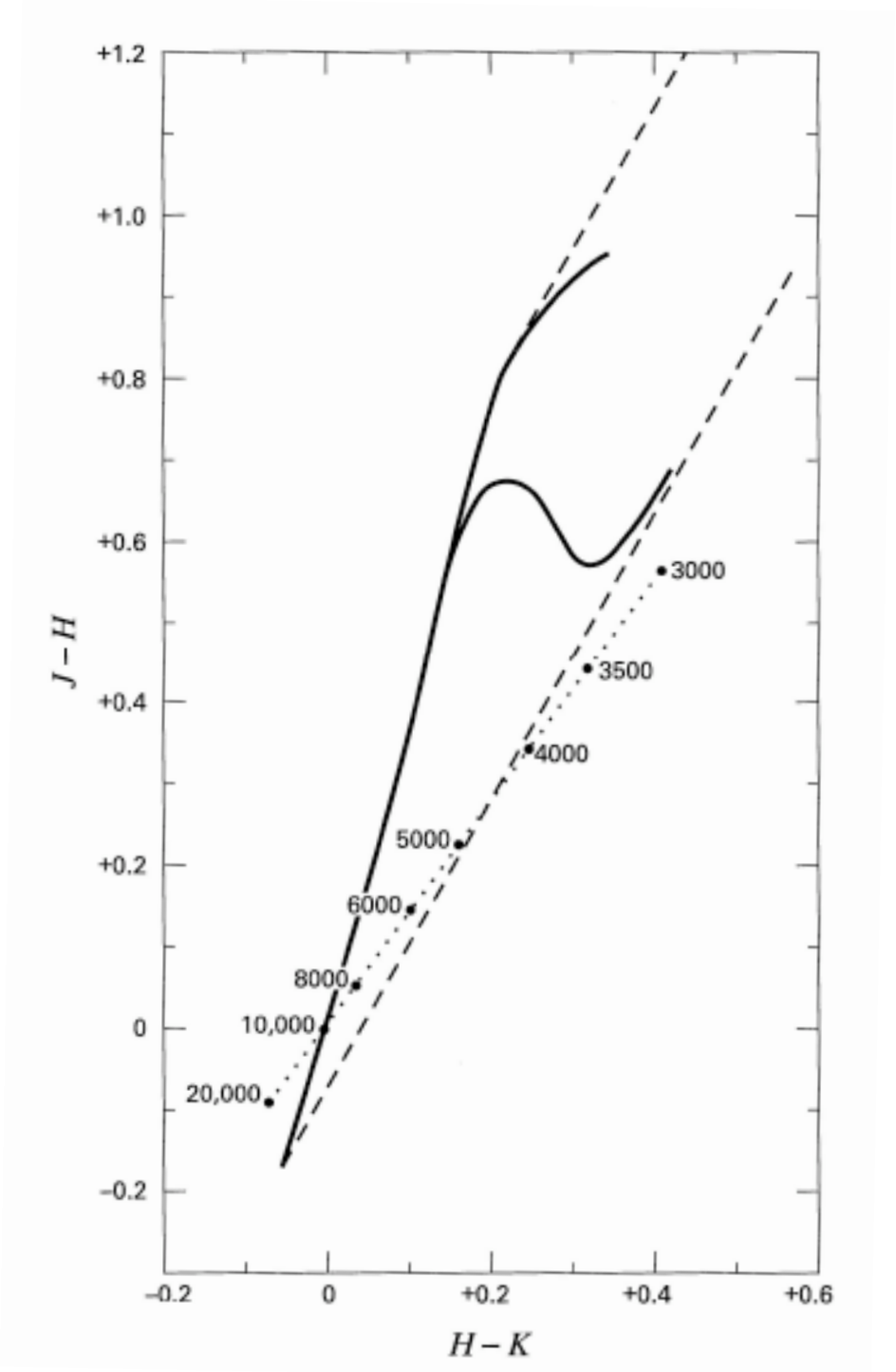

Figure 4.1 – Infrared color-color diagram. The solid curves are for main sequence stars (lower) and the giant branch (upper). The dotted line is for blackbodies of different temperatures. The broken lines indicate the relative reddening due to intervening dust.

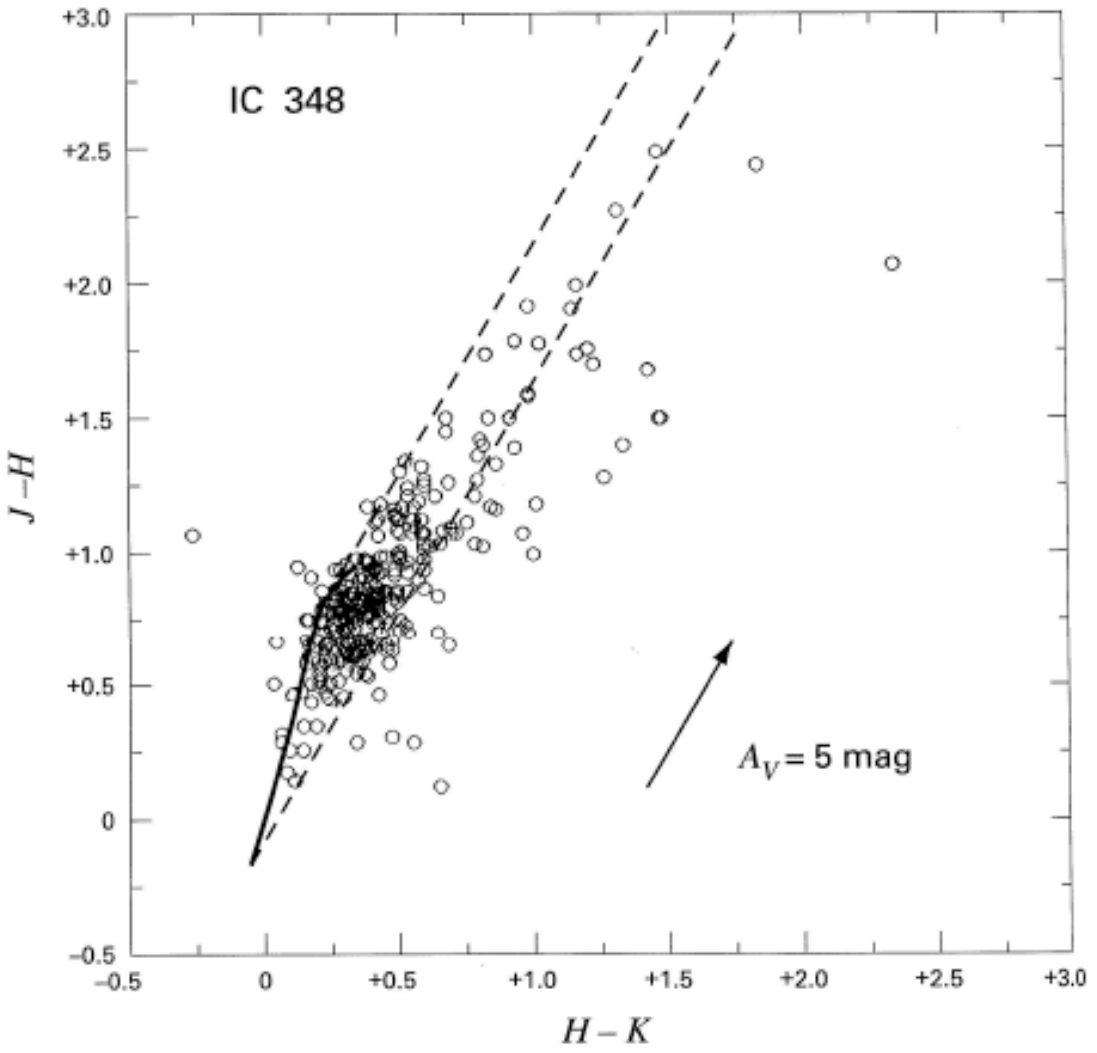

Figure 4.2 – The infrared color-color diagram for the IC 348 embedded cluster. Stars that fall below the lower broken line cannot be explained by reddening alone and, therefore, exhibit infrared excess.

The so-called **infrared spectral index** α_{IR} has been defined for that purpose

$$\alpha_{\text{IR}} \equiv \frac{d\left[\log\left(\lambda F_\lambda\right)\right]}{d\left[\log\left(\lambda\right)\right]}. \tag{4.3}$$

Using this equation we establish the following classes

- **Class I** protostars have $\alpha_{\text{IR}} > 0$
- **Class II** protostars have $-1.5 < \alpha_{\text{IR}} < 0$
- **Class III** protostars have $\alpha_{\text{IR}} < -1.5$.

Finally, when an object is so deeply embedded that it can only be detected at far-infrared and submillimetre wavelengths. It is said to belong to the **Class 0**. It follows from this classification that younger stars are associated with higher infrared excess and lower class numbers. Examples of spectral energy distributions for the different classes are shown in Figure 4.3 and Figure 4.4.

4.2 T, R, and OB Associations

The evolution of an embedded cluster will depend on the characteristics (e.g., the mass distribution) of its members (note that the different classes of protostars defined previously does not take the mass into account). We have already encountered examples T and OB associations in Chapter 1, we further add R associations to the list and review thair main characteristics.

4.2.1 T Associations

The members of a T association are low-mass stars; these associations contain no O or B stars, for example. The lack of massive stars implies that strong stellar winds and radiation fields will not quickly disperse the gas associated with the parent molecular clouds, as is the case for OB associations. In fact, it is likely that the observed distributions of stars from T associations in a complex are a fair representation of the initial dimensions of the parent cloud.

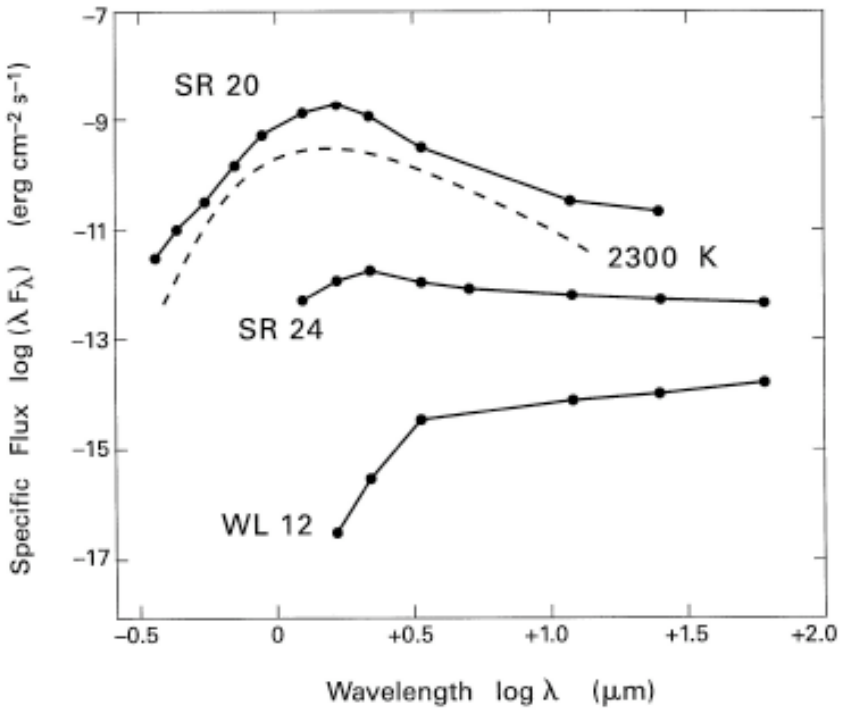

Figure 4.3 – Spectral energy distributions for Class I, II, and III sources in the ρ Ophiuchi dark cloud complex.

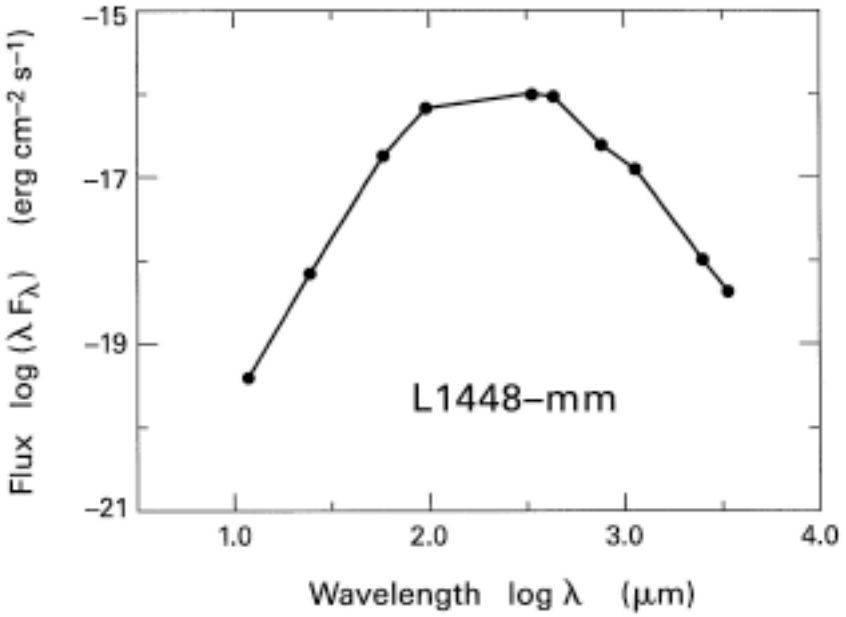

Figure 4.4 - Spectral energy distribution for the Class 0 source L1448-mm in Perseus.

The vast majority of stars within a T association are the so-called **T Tauri** stars ($< 2 M_{\odot}$). This group is further classified into two sub-groups: the **classical** and **weak-lined T Tauri stars**. Classical T tauri are identified through a spectroscopy that shows strong optical emission in Hα, and in the H and K-lines of Ca II at 3968 Å and 3934 Å, respectively. Weak-lined T Tauri stars lack in strong emission lines. Both sub-groups overlap significantly in age. A map of nearby T associations and embedded clusters in the Galaxy are presented in Figure 4.5. It should be noted that all of these regions include objects that are both obscured by dust or visible. This is evident from Figure 4.6 for the Taurus-Auriga complex, which shows a mixture of gas (therefore dust) and stars. A sign that embedded and visible objects (stars) coexist in such clouds.

4.2.2 **R Associations**

Besides the T Tauri and other low-mass stars in T associations there is another population of stars of intermediate-mass ($2 - 8 M_{\odot}$, A and B spectral types) that populate the so-called **R associations**. Although the Herbig Ae/Be stars exhibit strong emission lines (like classical T Tauri stars), most intermediate-mass are close to the ZAMS and are, therefore, lacking in that respect. Closeness to the ZAMS implies that the evolution from dense core to the main sequence through gravitational contraction happens relatively quickly (see Figure 1.11). This has for effect that these stars will not have time to stray far away from their parent molecular clouds and will, therefore, be the radiation sources for **reflection nebulae**, thus the name for these associations. Finally, we should also note that these intermediate-mass stars, which are spread out over approximately 10 pc, are always accompanied by a large number of low-mass stars. A list of nearby R associations with their individual count of B stars is given in Table 4.1.

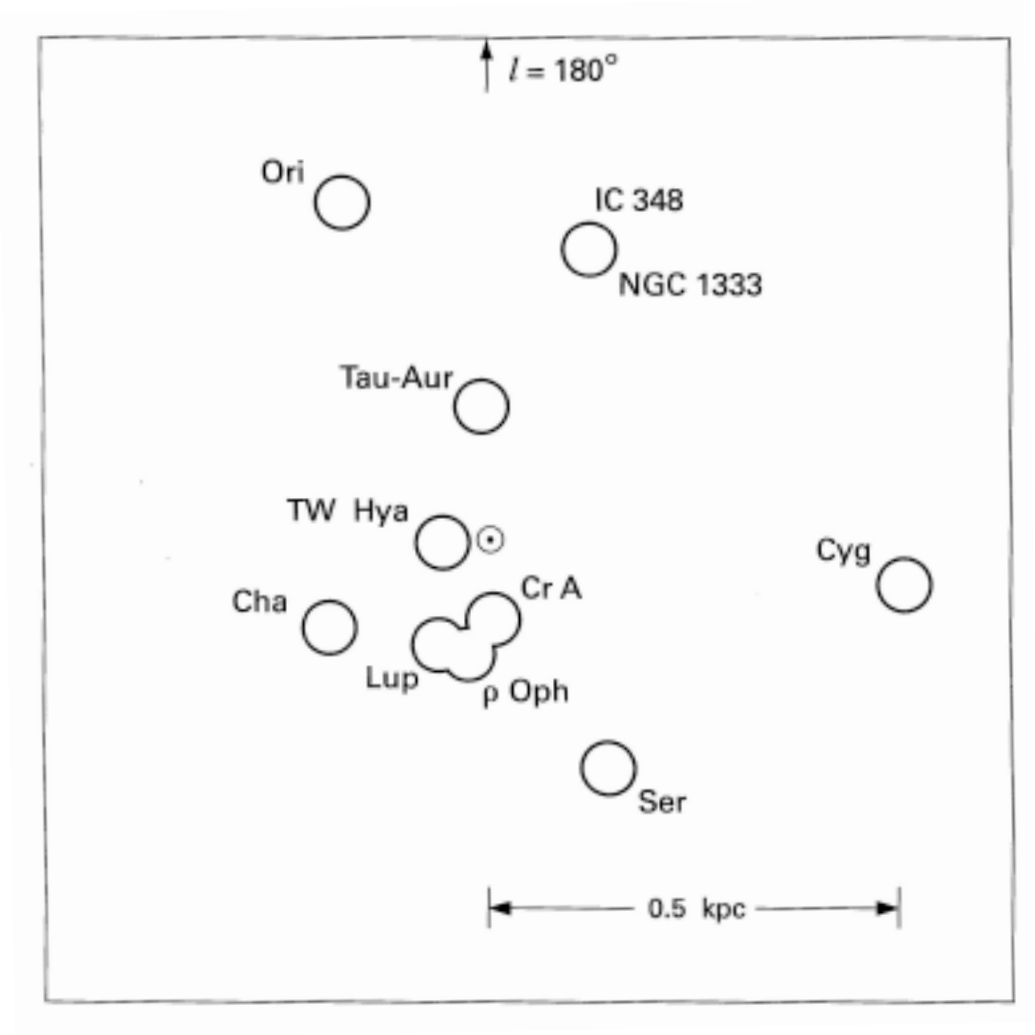

Figure 4.5 – Distribution of nearby T associations and embedded clusters in the Galaxy.

4.2.3 **OB Associations**

As their name implies OB associations harbor a number of O and (mostly) early-B stars capable of ionizing their surroundings and create HII regions. The size of these associations can vary greatly as is made clear by Table 4.2, which gives a list of nearby OB associations. This can be understood by the large internal velocities (on the order of 4 km/s) that characterize these systems and eventually lead to their expansion and dispersion. It follows that the older associations are also the largest.

The short lifetime of O and B stars (see Table 1.1) explains why they are mostly found in the vicinity of their parent molecular clouds. It follows that OB associations are good tracers of the Galactic spiral arms. The distribution of the closest OB associations is shown in Figure 4.7

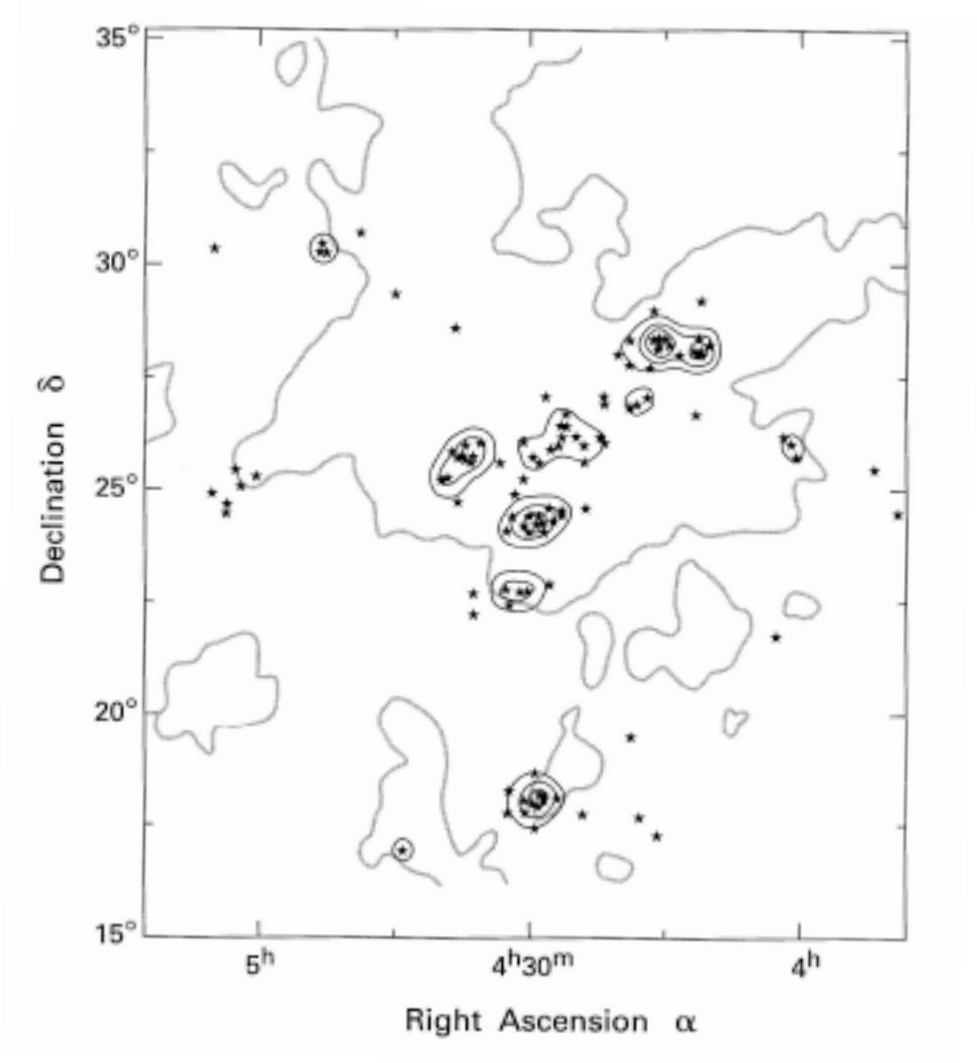

Figure 4.6 – Clusters of stars in Taurus-Auriga. The dark contours represent the stellar surface density, while the lighter contours are for the CO emission intensity. The mixture of gas (and therefore dust) and stars within this complex is telling of the fact that embedded and visible objects (stars) coexist in such clouds.

It can be seen from Figure 4.7 that there exists a huge ring of gas and stars (approximately 700 pc in diameter) that links many of the closest OB associations. This is the so-called **Gould's belt**. These linked associations have velocities that imply an outward expansion of the Gould's belt.

4.3 The Initial Mass Function

We have already mentioned on a few occasions that the associations of stars containing more massive stars (R and OB associations) also always harbor a much larger number of low-mass stars. We would, therefore, expect that censuses of field stars, star clusters, or associations to show that fact.

Table 4.1 – Nearby R Associations

Name	Distance (pc)	B Stars
Taurus R1	110	4
Taurus R2	140	2
Scorpius R1	150	9
Perseus R1	330	4
Taurus-Orion R1	360	5
Cepheus R2	400	5
Vela R1	460	3
Cassiopeia R1	530	5
Orion R1/R2	470	6
Cepheus R1	660	3
Canis Maior R1	690	8
Monoceros R1	800	4
Monoceros R2	830	7
Vela R2	870	6
Scorpius R5	870	4

One way to verify this is to measure the general luminosity function $\Phi(M_V)$, which gives $\Phi(M_V)\Delta M_V$ the number of stars per cubic parsec with absolute visual magnitude $M_V \pm \Delta M_V/2$ in the solar neighborhood. The result of such an endeavor is presented in Figure 4.8. It is, however, more illuminating to express $\Phi(M_V)$ as a function of the **initial luminosity function** $\psi(M_V)$, the relative frequency with which stars of different M_V appear, and the total Galactic star formation rate per square parsec $\dot{m}_*$.

Table 4.2 – Nearby OB Associations

Name	Distance (pc)	Diameter (pc)	O Stars	B Stars
Lower Centaurus-Crux	120	50	0	42
Upper Centaurus-Lupus	140	75	0	66
Upper Scorpius	150	30	0	49
α Persei (Perseus 3)	180	10	0	30
Casssiopeia-Taurus	210	200	0	83
Cepheus 6	270	40	0	6
Perseus 2	320	50	0	17
Trumpler 10	360	45	0	22
Lacerta 1	370	60	1	35
Vela 1	410	75	1	81
Orion 1	470	75	9	327
Collinder 121	590	120	2	85
Cepheus 2	610	110	1	53

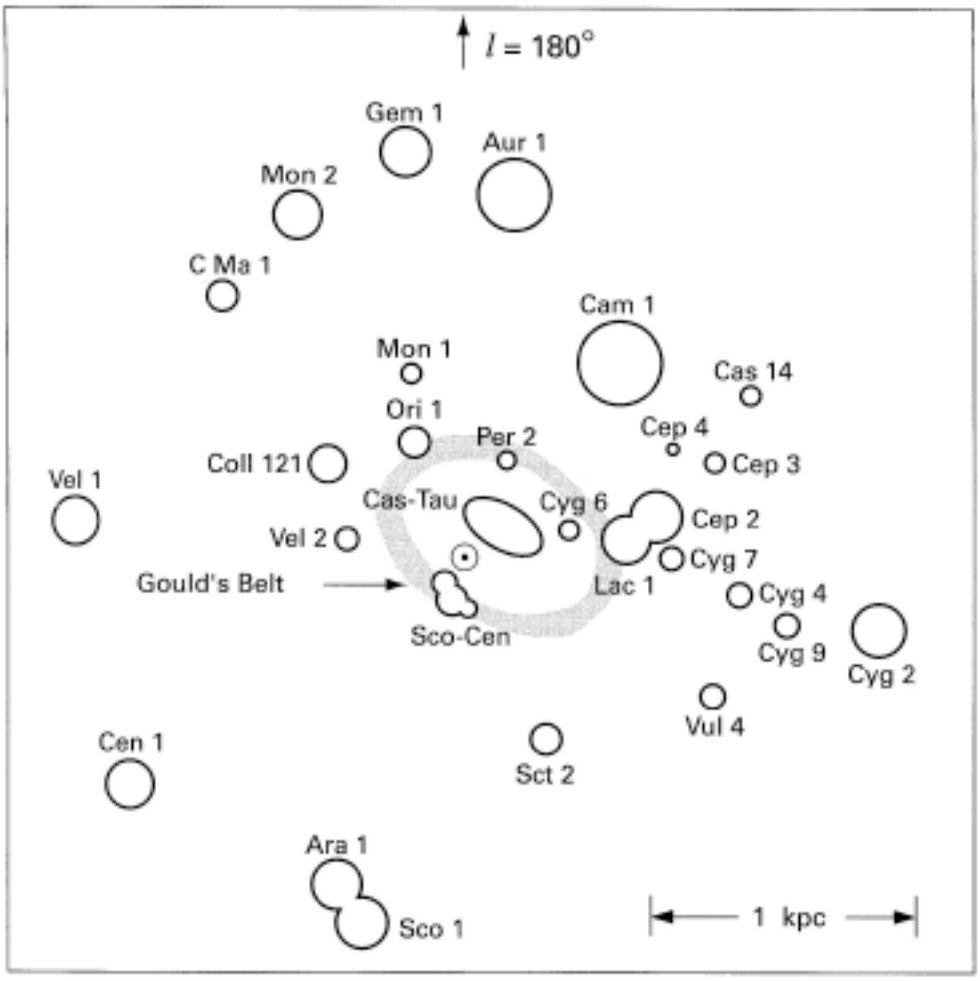

Figure 4.7 – Distribution of the nearest OB associations. The Sun is shown in near the centre of the map. The gray ring encompassing the Sun and the Cassiopeia-Taurus association indicates the position of the Gould's belt.

We, therefore, write

$$\Phi\left(M_V\right)=\begin{cases}\int_{t_{\rm gal}-t_{\rm ms}}^{t_{\rm gal}}\dot{m}_*\psi\left(M_V\right)\left[2H\left(M_V\right)\right]^{-1}dt, & \text{if } M_V < M_V^* \\ \int_{0}^{t_{\rm gal}}\dot{m}_*\psi\left(M_V\right)\left[2H\left(M_V\right)\right]^{-1}dt, & \text{if } M_V \geq M_V^*\end{cases} \tag{4.4}$$

where M_V^* is the absolute visual magnitude of stars for which $t_{\rm ms}=t_{\rm gal}$ ($t_{\rm gal}$ is the age of the Galaxy). The divisions by the scale height $H\left(M_V\right)$ accounts for the fact that stars of different mass (and magnitude) have densities that differ away from the Galactic plane. This factor is accounted for by the fact that vertical dependency of the star density is assumed to be $e^{-|z|/H(M_V)}$; integration from minus to plus infinity yields $2H\left(M_V\right)$.

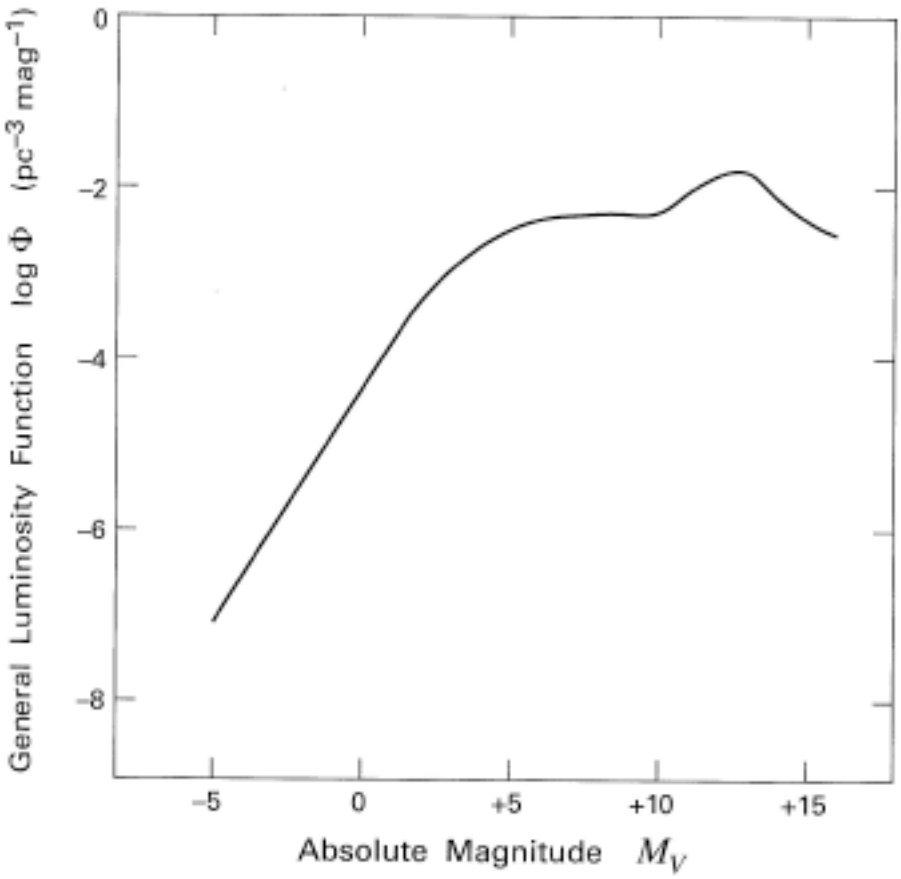

Figure 4.8 – General luminosity function for stars in the solar neighborhood.

We also require that

$$\int \psi(M_V)\, dM_V = 1. \tag{4.5}$$

Equations (4.4) can be inverted, starting from the graph of Figure 4.1, to determine $\psi(M_V)$. Determination of the **initial mass function** $\xi(M_*)$ is then easily obtained with

$$\xi(M_*) = \psi(M_V)\frac{dM_*}{dM_V}, \tag{4.6}$$

where M_* stands for stellar mass. The so-called **Salpeter's power law** thus derived yielded

$$\xi(M_V) \propto M_*^{-2.35}. \tag{4.7}$$

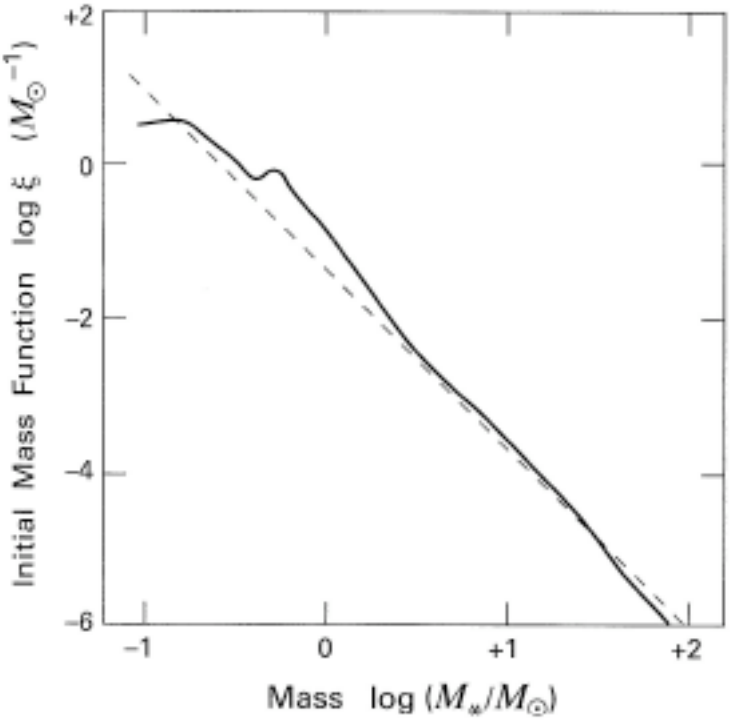

Figure 4.9 – The initial mass function for solar neighborhood stars. The broken line shows Salpeter's power law.

More recent results give the more complicated relations

$$\xi(M_*) = \begin{cases} C\left(\dfrac{M_*}{M_\odot}\right)^{-1.2}, & 0.1 < \dfrac{M_*}{M_\odot} < 1.0 \\ C\left(\dfrac{M_*}{M_\odot}\right)^{-2.7}, & 1.0 < \dfrac{M_*}{M_\odot} < 10 \\ 0.4C\left(\dfrac{M_*}{M_\odot}\right)^{-2.3} & 10 < \dfrac{M_*}{M_\odot} \end{cases} \tag{4.8}$$

where C is a normalization constant. The result obtained from Figure 4.8 is shown in Figure 4.9. The aforementioned dominance of low-mass stars in the solar neighborhood is made clear from the figure. More precisely, if it is found that 70% of stars have $M_* \geq 0.1 M_\odot$, only 12% have $M_* > 1 M_\odot$ and 0.3% have $M_* > 10 M_\odot$.

Another interesting result is that open and association clusters also show the same sort of initial mass function; examples are shown in Figure 4.10. Neither the apparent universality nor the functional form of the initial mass function $\xi(M_*)$ is well understood.

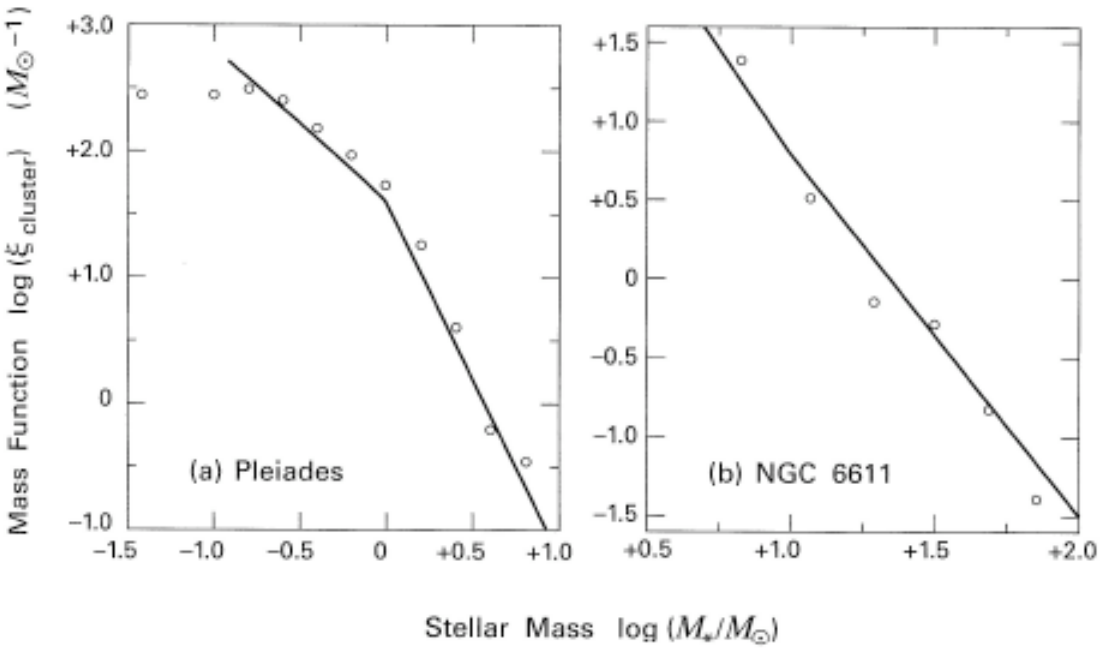

Figure 4.10 – Initial mass functions for the Pleiades (left) and the OB association of NGC 6611.